Journal of Energy Chemistry 98 (2024) 472–480

Contents lists available at ScienceDirect

Journal of Energy Chemistry

journal homepage: www.elsevier.com/locate/jechem

http://www.journals.elsevier.com/journal-of-energy-chemistry/

Dynamic in situ reconstruction of $NiSe_2$ promoted by interfacial $Ce_2(CO_3)_2O$ for enhanced water oxidation

Fengli Wei [a], Jinghao Shen [a], Jiayin Xie [a], Zuyang Luo [a], Luyan Shi [a], Tayirjan Taylor Isimjan [b], Xiulin Yang [a,*], Jieshan Qiu [c,*], Bin Wu [d,e,*]

[a] Guangxi Key Laboratory of Low Carbon Energy Materials, School of Chemistry and Pharmaceutical Sciences, Guangxi Normal University, Guilin 541004, Guangxi, China
[b] Saudi Arabia Basic Industries Corporation (SABIC) at King Abdullah University of Science and Technology (KAUST), Thuwal 23955-6900, Saudi Arabia
[c] State Key Laboratory of Chemical Resource Engineering, State Key Laboratory of Organic-Inorganic Composites, College of Chemical Engineering, Beijing University of Chemical Technology, Beijing 100029, China
[d] Helmholtz-Zentrum Berlin für Materialien und Energie GmbH, Albert-Einstein-Straße 15, Berlin 12489, Germany
[e] Institute of Physics, Humboldt University Berlin, Newton-Straße 15, Berlin 12489, Germany

ARTICLE INFO

Article history:
Received 3 June 2024
Revised 28 June 2024
Accepted 30 June 2024
Available online 3 July 2024

Keywords:
Dynamic reconstruction
Oxygen evolution reaction
Heterostructure
In situ characterization
Density functional theory

ABSTRACT

Understanding and manipulating the structural evolution of water oxidation electrocatalysts lays the foundation to finetune their catalytic activity. Herein, we present a synthesis of $NiSe_2$-$Ce_2(CO_3)_2O$ heterostructure and demonstrate the efficacy of interfacial $Ce_2(CO_3)_2O$ in promoting the formation of catalytically active centers to improve oxygen evolution activity. In-situ Raman spectroscopy shows that incorporation of $Ce_2(CO_3)_2O$ into $NiSe_2$ causes a cathodic shift of the $Ni^{2+}\rightarrow Ni^{3+}$ transition potential. Operando electrochemical impedance spectroscopy reveals that strong electronic coupling at heterogeneous interface accelerates charge transfer process. Furthermore, density functional theory calculations suggest that actual catalytic active species of NiOOH transformed from $NiSe_2$, which is coupled with $Ce_2(CO_3)_2O$, can optimize electronic structure and decrease the free energy barriers toward fast oxygen evolution reaction (OER) kinetics. Consequently, the resultant $NiSe_2$-$Ce_2(CO_3)_2O$ electrode exhibits remarkable electrocatalytic performance with low overpotentials (268/304 mV @ 50/100 mA cm^{-2}) and excellent stability (50 mA cm^{-2} for 120 h) in the alkaline electrolyte. This work emphasizes the significance of modulating the dynamic changes in developing efficient electrocatalyst.

1. Introduction

Electrochemical water splitting to generate green hydrogen stands out as a promising avenue for renewable energy conversion and storage, as well as achieving carbon neutrality [1,2]. Current hindrance mainly originates from the multiple proton-coupled electron transfer steps in anodic oxygen evolution reaction (OER), necessitating significant overpotential to surmount its sluggish reaction kinetics [3–5]. In this regard, an appropriate catalyst is essential to accelerate the OER for enhancing energy conversion efficiency. While precious metal-based catalysts like IrO_2 and RuO_2 are the most active OER catalysts, their scarcity and poor long-term stability limit industrial application [6]. Therefore, developing highly active and stable nonprecious OER electrocatalysts is of pressing relevance for practical water-splitting applications.

Recently, transition metal selenides (TMS) have emerged as a propitious candidate due to their favorable conductivity, tunable electronic structure, and low cost [7,8]. With insights into the OER process, TMS generally undergo dynamic self-reconstruction under oxidizing potentials to form metal oxides/(oxy)hydroxides, which exhibit significantly enhanced OER activity compared with directly synthesized oxide/(oxy)hydroxide counterparts [9–11]. For instance, Niu et al. verified that FeSe nanosheets underwent in situ phase transformation to active FeOOH species [12]. Hu's group also reported that $Ni_xFe_{1-x}Se_2$ transformed into corresponding hydroxides during electrochemical cycling process, showing superior OER performance [13]. These results have demonstrated that the reconstruction-derived metal oxy-hydroxide (MOOH) is the origin of high catalytic activity. Hence, seeking reasonable

* Corresponding authors.
E-mail addresses: xlyang@gxnu.edu.cn (X. Yang), qiujs@mail.buct.edu.cn (J. Qiu), bin.wu@helmholtz-berlin.de (B. Wu).

https://doi.org/10.1016/j.jechem.2024.06.048

strategies to promote the in-situ formation of active (oxy)hydroxides is crucial. During the dynamic reconstruction process, metal sites undergo oxidation, accompanied by the adsorption of oxygen species and/or deprotonation of hydroxyl [14]. Accordingly, structure evolution is intricately linked to the chemical affinity between metal sites and oxygen species, which can be subtly tuned by altering electronic states [15]. Heterogeneous multi-junction catalysts typically possess superior activities compared to single-metal catalysts, as the interfacial interactions can efficiently modulate electron transfer and optimize local coordination environment of active sites and reaction intermediates adsorption/desorption behaviors, thus facilitating conversion of active species during surface reconstruction [16–19]. Xu's work indicated that Mott-Schottky heterojunction promoted the surface reconstruction of $NiSe_2/MoSe_2$ to form NiOOH as the actual active site [20]. Jiang and colleagues unveiled that in Ni_2P/FeP heterostructures, Ni could increase the bond strength of superficial Fe–O and accelerate the formation of high active FeOOH phase during OER, which is response for enhancing catalytic performance [21]. Li et al. employed interface interactions to design the FeOOH@NiFe (layered double hydroxide, LDH) heterostructure [22], where the abundant heterogeneous interface between FeOOH and NiFe LDH promoted electron transfer, expeditiously inducing the reconstruction of NiFe LDH into Ni(Fe)OOH. Therefore, constructing heterogeneous structures is an advantageous strategy for promoting the reconstruction.

Although the concept of heterostructure engineering appears straightforward, selecting components necessitates rigorous and meticulous deliberation. Ce, as one of the most abundant rare-earth elements, features excellent redox properties, stable crystal structure, and good electronic/ionic conductivity [23]. Therefore, the addition of Ce can greatly improve the OER performance by tuning the microstructure including the electronic state of transition metal ions, defect type and concentration, and the binding energy of the intermediates [24]. Recently, Ce compounds have demonstrated their efficacy as co-catalysts in facilitating dynamic reconfiguration by forming robust heterointerfaces with host surfaces [25,26]. In situ Raman identified that the CeO_2 additives accelerated the structural transformation of NiO, Ni_3S_2 [27], and $CoS_{1.97}$ [28] to active (oxy)hydroxide species towards efficient OER. Such promotion is not unique to CeO_2, but also potentially presents in $Ce_2(CO_3)_2O$, which has attracted great attention due to its distinct phase structures and morphologies [29]. In particular, our group previously highlighted the substantial enhancement in electrocatalytic activity and efficiency achieved by combining $Ce_2(CO_3)_2O$ with CoP [30]. Based on the above inspiring achievements, interfacial $Ce_2(CO_3)_2O$ is highly anticipated to hasten the formation of catalytically active centers by activating reconstruction process in TMS, thereby systematically boosting the OER performance.

In this work, we have synthesized for the first time $NiSe_2$-$Ce_2(CO_3)_2O$ heterojunction uniformly grown on carbon cloth, which is used as a self-supported electrode for the highly efficient OER. The dynamic evolution of surface structure of $NiSe_2$-$Ce_2(CO_3)_2O$ and the transformation of active center/intermediate are confirmed by the comprehensive use of various in-situ characterization techniques. The formation of interfacial $Ce_2(CO_3)_2O$ not only facilitates the activation of structure reconstruction into true catalytic activity centers at reduced potential, but also accelerates charge transfer. Meanwhile, density functional theory (DFT) calculations show that interfacial $Ce_2(CO_3)_2O$ can greatly optimize electronic structure of $NiOOH/Ce_2(CO_3)_2O$ and the Gibbs free energy of OER pathways. In summary, experiments and theoretical calculations demonstrate that the establishment of heterostructure optimizes the coordination environment and facilitates the activation of dynamic reconstruction into true catalytic active centers at lower potential, thereby boosting electrocatalytic activity. As a result, the optimized catalyst exhibits excellent OER activity with overpotentials (additional voltage applied above thermodynamic requirements to drive electrochemical reactions) of 268 and 304 mV at 50 and 100 mA cm^{-2} respectively, and good long-term stability in 1.0 M KOH. Furthermore, the alkaline electrolyzer assembled with the $NiSe_2$-$Ce_2(CO_3)_2O$ as anode and Pt/C as cathode achieves a current density of 100 mA cm^{-2} at a low voltage of 1.65 V, as well as substantial endurance. Our study spotlights the interfacial engineering inducing the highly active NiOOH during OER, which is expected to inspire the mechanistic understanding of OER and shed some light on catalyst design.

2. Experimental

2.1. Reagents and materials

The materials in this work include nickel (II) nitrate hexahydrate ($Ni(NO_3)_2{\cdot}6H_2O$, 99%, Xilong), cerium nitrate hexahydrate ($Ce(NO_3)_2{\cdot}6H_2O$, 99.5%, Aladdin), selenium (Se, 99.9%, Aladdin), potassium hydroxide (KOH, 90%, Macklin), sodium borohydride ($NaBH_4$, 98.0%, Sinopharm Group), ethylene glycol ($C_2H_6O_2$, 99.9%, Xilong), nitric acid (HNO_3, 68%, Kelong), Nafion (5 wt%, Alfa Aesar), commercial Pt/C (20 wt% Pt, Sinero), and carbon cloth (CC, Kunshan). RuO_2 powder was synthesized by directly annealing $RuCl_3{\cdot}3H_2O$ (37%, Inno-chem) at 400 °C in air. All chemicals were used as received without further purification.

2.2. Synthesis of NiCeCHO

The NiCeCHO was in-situ grown on CC by a hydrothermal method. In detail, a piece of CC (2 cm × 3 cm) was initially cleaned with HNO_3, and then washed alternately with deionized (DI) water and ethanol. 0.51 g (1.75 mmol) $Ni(NO_3)_2{\cdot}6H_2O$, 0.38 g (0.875 mmol) $Ce(NO_3)_3{\cdot}6H_2O$, and 0.525 g urea were dissolved into 30 mL aqueous solution, which was then sealed in a 50 mL Teflon-lined autoclave. After immersing the pretreated CC into the homogenous solution, the autoclave was maintained at 120 °C for 10 h. The precursor on CC (denoted as NiCeCHO) was successfully synthesized after washing by deionized water several times and drying in the 60 °C oven overnight.

2.3. Synthesis of $NiSe_2$-$Ce_2(CO_3)_2O$

Initially, 0.12 g (1.5 mmol) Se powder and 0.13 g (3.4 mmol) $NaBH_4$ were added into 10 mL deionized water to form solution **A**. Mixing 10 mL deionized water with 10 mL ethylene glycol results in the formation of solution **B**. Then solutions **A** and **B** were mixed and stirred for 1 h together to form a homogeneous mixture. The mixture was poured into a 50 mL Teflon-lined stainless-steel autoclave containing the NiCeCHO. The autoclave was sealed and maintained at 180 °C for 10 h. After cooling to room temperature, the product (denoted as $NiSe_2$-$Ce_2(CO_3)_2O$) was washed with deionized water and ethanol several times and then dried at 60 °C. Following the same line of thought, a series of samples with different ratios of Ni/Ce (1/2, 1.5/1.5, 3/0, and 0/3) were synthesized with the same method.

2.4. Fabrication of RuO_2 and 20 wt% Pt/C electrodes

2 mg RuO_2 or 20 wt% Pt/C was dispersed into a mixture comprising 50 μL DI water, 150 μL ethanol, and 5 μL 5 wt% Nafion, respectively. The mixture was ultrasonicated for 30 min, and the resulting slurry was then applied onto a CC substrate, which was dried under ambient condition.

3. Results and discussion

3.1. Synthesis strategy and structural analysis

The self-supported $NiSe_2$-$Ce_2(CO_3)_2O$ electrode, as schematically shown in Fig. 1(a), was synthesized through an accessible two-step hydrothermal method. Initially, the detailed morphological evolution of the samples is tracked by scanning electron microscopy (SEM). In a typical synthesis, the NiCeCHO precursor is initially obtained via in-situ growth in aqueous solvents. As depicted in Fig. S1(a and b), NiCeCHO exhibits a morphology of downy nanorods, uniformly grown on a smooth CC substrate. After selenization, the resulting $NiSe_2$-$Ce_2(CO_3)_2O$ legibly delineates rice-granular structure composed of protuberant nanoparticles firmly anchored on the CC, imparting higher stability to the $NiSe_2$-$Ce_2(CO_3)_2O$ (Fig. 1b). In addition, pure $NiSe_2$ showcases the typical microspherical morphology (Fig. S1c). Pure $Ce_2(CO_3)_2O$ in Fig. S1(d) features the characteristics of interspersed sparse nanospheres cross with abundant nanorods. As shown in Fig. 1(c), transmission electron microscopy (TEM) images further confirm that the $NiSe_2$-$Ce_2(CO_3)_2O$ possesses a unique rice-granular morphology, in accordance with the SEM observations. Fig. 1(d) presents a high-resolution TEM image (HRTEM) of $NiSe_2$-$Ce_2(CO_3)_2O$. Thereinto, the well-resolved lattice fringes with the interplanar distances of 0.298, 0.308, and 0.576 nm are assigned to cubic $NiSe_2$ (200) plane, orthorhombic $NiSe_2$ (020) plane, and $Ce_2(CO_3)_2O$ (011) plane, respectively, preliminarily confirming the successful preparation of $NiSe_2$-$Ce_2(CO_3)_2O$ heterostructure. The high-angle annular dark-field scanning transmission electron microscopy (HAADF-STEM) image and the corresponding energy dispersive spectrometer (EDS) elemental mapping images of $NiSe_2$-$Ce_2(CO_3)_2O$ demonstrate the homogeneous distribution of Ni, Ce, Se, O, and C elements over the entire heterostructure (Fig. 1e). Moreover, the inductively coupled plasma mass spectrometry (ICP-MS) analysis shows the detailed loading of different electrocatalysts. Thereinto, the $NiSe_2$-$Ce_2(CO_3)_2O$ catalyst comprises Ni (23.09 wt%/1.41 mg cm^{-2}) and Ce (7.3 wt%/0.45 mg cm^{-2}) (Table S1).

The crystallographic texture of the obtained catalysts was elucidated by X-ray diffraction (XRD) patterns. The XRD patterns provided in Fig. S2(a) confirm that the strong peaks of NiCeCHO match the signals of $Ni_2CO_3(OH)_2{\cdot}H_2O$ (JCPDS: 29-0868) and $Ce_2(CO_3)_2O$ (JCPDS: 43-0602). After selenization, the diffraction

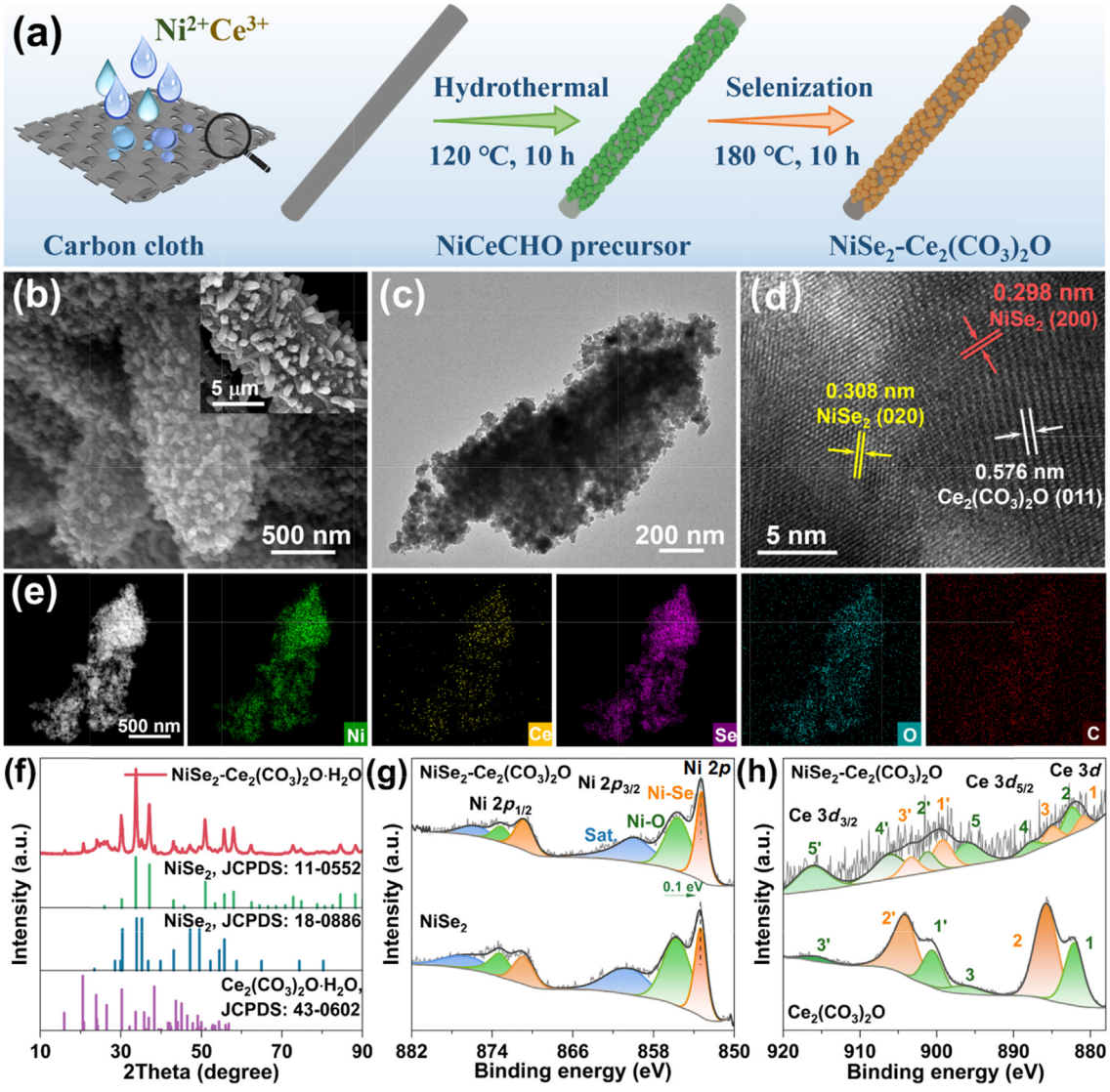

Fig. 1. Synthesis process and microscopy characterization. (a) Schematic diagram for the fabrication of $NiSe_2$-$Ce_2(CO_3)_2O$. (b) SEM of $NiSe_2$-$Ce_2(CO_3)_2O$. (c) TEM and (d) HRTEM of $NiSe_2$-$Ce_2(CO_3)_2O$. (e) EDS mapping of Ni, Ce, Se, O, and C elements in $NiSe_2$-$Ce_2(CO_3)_2O$. (f) XRD pattern of $NiSe_2$-$Ce_2(CO_3)_2O$. High-resolution XPS spectra of (g) Ni 2*p* and (h) Ce 3*d* regions in $NiSe_2$-$Ce_2(CO_3)_2O$, $NiSe_2$, and $Ce_2(CO_3)_2O$.

peaks of $NiSe_2$-$Ce_2(CO_3)_2O$ in Fig. 1(f) are corresponded well with cubic $NiSe_2$ (JCPDS: 11-0552), orthorhombic $NiSe_2$ (JCPDS: 18-0886), and $Ce_2(CO_3)_2O$ (JCPDS: 43-0602), in good accordance with the HRTEM results. It is noteworthy that $Ce_2(CO_3)_2O$ remains unaltered, as transformations only occur when calcined at 400 °C [30]. Meanwhile, the single $NiSe_2$ catalyst also manifests two distinct crystallographic phases of $NiSe_2$ (Fig. S2b). Additionally, Fig. S2(c) confirms the formation of pure $Ce_2(CO_3)_2O$ (JCPDS: 43-0602). The valence states of the surface metal species were further examined by X-ray photoelectron spectroscopy (XPS). The survey spectrum (Fig. S3) clearly corroborates the coexistence of Ni, Ce, Se, O, and C elements in $NiSe_2$-$Ce_2(CO_3)_2O$. As shown in Fig. S4(a), the high-resolution C 1*s* XPS spectrum of $NiSe_2$-$Ce_2(CO_3)_2O$ catalyst is deconvolved into C=C (284.0 eV), C–C (284.8 eV), C–O (285.8 eV), and C=O (286.6 eV) [31]. Within the Ni 2*p* spectral range for $NiSe_2$-$Ce_2(CO_3)_2O$, the peaks centered at 853.25 and 870.76 eV can be assigned to nickel selenide, which shows a marginally downward shift relative to pure $NiSe_2$ [32]. Additionally, the spin-orbit doublets at 855.55 and 873.06 eV, along with satellite peaks, are characteristic of nickel in an oxidized state, likely a consequence of unavoidable surface exposure to atmospheric oxygen (Fig. 1g) [26,33]. Regarding the Ce 3*d* core level spectra, notably different peak patterns can be observed in $NiSe_2$-$Ce_2(CO_3)_2O$ and pure $Ce_2(CO_3)_2O$, suggesting distinct alterations in the local electronic environment of Ce caused by the construction of heterostructure (Fig. 1h). The Ce 3*d* spectrum of $NiSe_2$-$Ce_2(CO_3)_2O$ is fitted with five pairs of spin-energy separations. The characteristic peaks located at 881.02, 885.07 eV (1, 3) and 899.27, 903.37 eV (1, 3) are assigned to Ce^{3+} ($3d^{10}4f^1$), whereas the six peaks at 882.42, 887.87, 895.97 eV (2, 4, 5) and 901.23, 906.17, 916.17 eV (2, 4, 5) are attributed to Ce^{4+} ($3d^{10}4f^0$), demonstrating the existence of Ce^{3+} and Ce^{4+} [34]. The Ce 3*d* spectrum in pure $Ce_2(CO_3)_2O$ clearly could be deconvoluted into three series of subpeaks. The two peaks at 885.77 and 904.01 eV (2, 2) are attributed to Ce^{3+}. Additionally, the peaks at 882.1, 896.35 eV (1, 3) and 900.49, 915.64 eV (1, 3) are attributed to the oxidation states of Ce^{4+} [30,35]. Based on the above results, valence shifts of Ni and discernible changes in the local electronic environment of Ce conjointly bear out the substantial electronic coupling between them, which effectually optimize the electronic structure and the adsorption energy of reaction intermediates, thus ameliorating catalytic activity [36]. In the Se region, the peaks at 54.98 and 55.88 eV are attributed to the Se $3d_{5/2}$ and Se $3d_{3/2}$ orbitals of Ni–Se, respectively, and a peak at 59.24 eV confirms the presence of oxidized selenium species (SeO_x) on the surface (Fig. S4b) [37,38].

3.2. Electrocatalytic OER performance

A standard three-electrode setup was employed to assess the electrocatalytic performance of $NiSe_2$-$Ce_2(CO_3)_2O$ for the OER in 1.0 M KOH solution. As shown in Fig. 2(a), the linear sweep voltammetry (LSV) curves demonstrate the exceptional OER activity of $NiSe_2$-$Ce_2(CO_3)_2O$ with only 268, 304, and 335 mV required to deliver the current densities of 50, 100, and 200 mA cm^{-2}, respectively, surpassing other tested catalysts. Further insights into the kinetic mechanism are gleaned from the Tafel plot. The Tafel slope for $NiSe_2$-$Ce_2(CO_3)_2O$ stands at 86.2 mV dec^{-1}, markedly smaller than that of RuO_2 (96.4 mV dec^{-1}), $NiSe_2$ (130.0 mV dec^{-1}), and NiCeCHO (151.2 mV dec^{-1}), suggesting faster OER kinetics (Fig. 2b). The value of $\eta/\log|j|$ is a descriptor of the correlation between current density (j) and overpotential (η). A smaller $\eta/\log|j|$ ratio implies a lower hindrance to increasing current density [39,40]. Fig. 2(c) shows that $NiSe_2$-$Ce_2(CO_3)_2O$ maintains a smaller ratio than $NiSe_2$ under different current densities, further confirming its good reaction kinetics. The electrochemical double-layer capacitance (C_{dl}) values extracted from cyclic voltammetry (CV) are closely related with electrochemically active surface areas (ECSA). The $NiSe_2$-$Ce_2(CO_3)_2O$ manifests the higher values of C_{dl} (2.2 mF cm^{-2}) and ECSA (55.0 cm^2), unequivocally implying more active sites exposed (Fig. 2d and Figs. S5 andS6a). In order to exclude the influence of different mass loadings, the LSV curves are normalized by ECSA to compare their intrinsic activity. As demonstrated in Fig. S6(b), the ECSA-normalized current of $NiSe_2$-$Ce_2(CO_3)_2O$ is distinctly higher than that of others, demonstrating the excellent OER intrinsic activity. Therefore, the enhanced electrocatalytic activity of $NiSe_2$-$Ce_2(CO_3)_2O$ depends on the improved intrinsic activity of the metal sites rather than the size of the active area [41]. In addition, to explore the effect of Ni/Ce molar ratio on the OER activity, various samples with different ratios (Ni/Ce = 0, 0.5, 1, 2, and 3) were prepared. When Ni/Ce = 2, $NiSe_2$-$Ce_2(CO_3)_2O$ exhibits the best OER performance, which may result from the best synergistic effects via suitable Ce species introduction (Fig. S7). Moreover, OER activity of $NiSe_2$-$Ce_2(CO_3)_2O$ under acidic (0.5 M H_2SO_4) and neutral (1.0 M phosphate-buffered saline, PBS) conditions were studied. As illustrated in Fig. S8(a), $NiSe_2$-$Ce_2(CO_3)_2O$ fails to demonstrate appreciable OER performance under both 0.5 M H_2SO_4 and 1.0 M PBS. Considering that CeO_2 is the most prevalent Ce-based compound, we examined its effect on the OER properties of $NiSe_2$ and found that the OER activity of $NiSe_2$-CeO_2 is inferior to that of $NiSe_2$-$Ce_2(CO_3)_2O$ (Fig. S8b).

Stability is also a crucial parameter for evaluating high efficient electrocatalyst. $NiSe_2$-$Ce_2(CO_3)_2O$ maintains a consistent operation at 50 mA cm^{-2} over a duration of 120 h, with no discernible decay in activity (Fig. 2e), underscoring the outstanding durability in basic solution. We performed contact angle tests on synthesized materials to understand the impact of interfacial ion/molecule interactions on water adhesion. The contact angle of $NiSe_2$-$Ce_2(CO_3)_2O$ is 16.4°, which is apparently smaller than that of $NiSe_2$ (85.2°), indicative of the higher hydrophilicity of $NiSe_2$-$Ce_2(CO_3)_2O$ heterostructure electrode (inset in Fig. 2e). Such good hydrophilicity can obviously facilitate electrolyte wettability with electrocatalysts, thereupon favoring the transport of electrolyte within the electrode [42,43]. Impressively, $NiSe_2$-$Ce_2(CO_3)_2O$ surpasses other representative non-precious metal catalysts recently reported in terms of both OER overpotential and Tafel slope, as presented in Fig. 2(f) and Table S2.

3.3. Finite element method simulation

The hydrophilic and electrochemically-active interfacial layer between the electrocatalyst and electrolyte has been proved to play a significant role in the thermodynamic reaction kinetics of OER regarding that this reaction requires hydrophilic/aerophobic and rapidly electron/mass-transportable interfaces [44–46], which includes the electrical energy transfer and the energy-converted mass transfer [47]. The finite element method (FEM) simulation (see the Supporting Information for more details about computational method) was thus performed to investigate the transportation process during the oxygen production. Two models assigned to $NiSe_2$-$Ce_2(CO_3)_2O$ and $NiSe_2$ were constructed according to their interfacial water wettability, electrochemical impedance, and electrochemically active area. The geometric model used for the simulation is shown in Fig. S9. As exhibited in Fig. 3(a and e), it can be clearly noticed that the electrode using $NiSe_2$-$Ce_2(CO_3)_2O$ catalyst possesses the fastest oxygen production rate, which was well in line with the experimental results. It is worth noting that the bubble breakage in movement after the action of the electrode cell wall is an important process in the electrochemical oxygen production and mass transfer process. Concerning the bottom of the electrode is the gas production outlet, the generation and collapse of a large number of bubbles lead to the accelerated local gas flow rate, causing a speed difference in the surrounding relatively static elec-

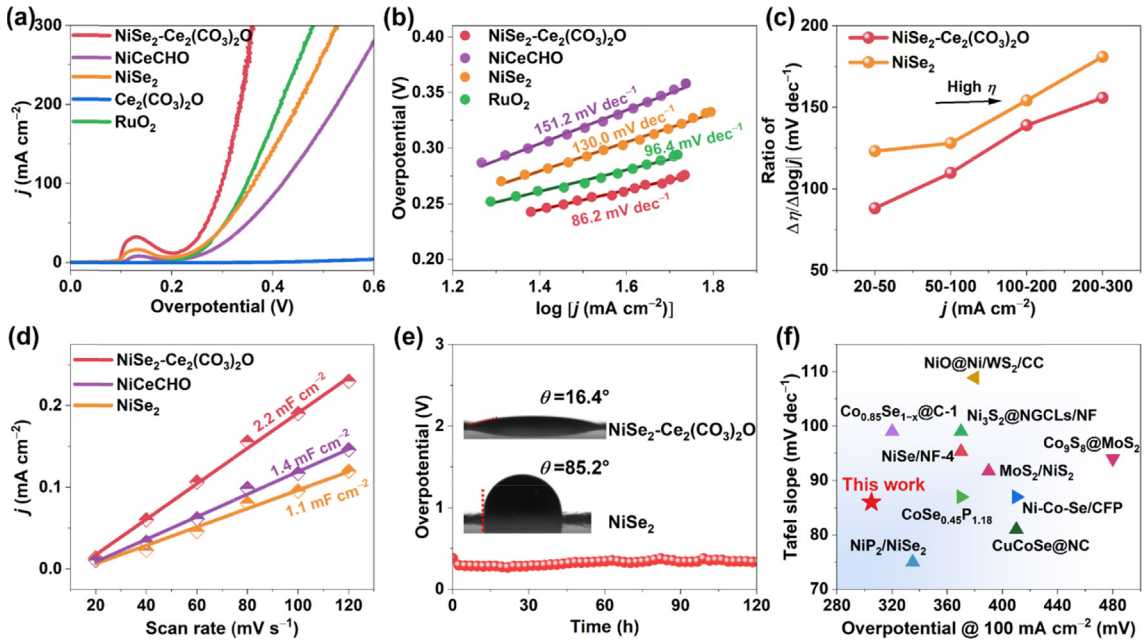

Fig. 2. Electrocatalytic OER properties of the catalysts recorded in 1.0 M KOH. (a) LSV polarization curves and (b) Tafel plots of various catalysts. (c) Ratio of $\eta/\log|j|$ at different current densities. (d) Double-layer capacitance (C_{dl}) plots. (e) Chronopotentiometry of $NiSe_2$-$Ce_2(CO_3)_2O$ at 50 mA cm^{-2} (the inset displays the contact angle test for $NiSe_2$-$Ce_2(CO_3)_2O$ and $NiSe_2$. (f) Comparison of overpotentials at 100 mA cm^{-2} and Tafel slopes for previously reported OER catalysts.

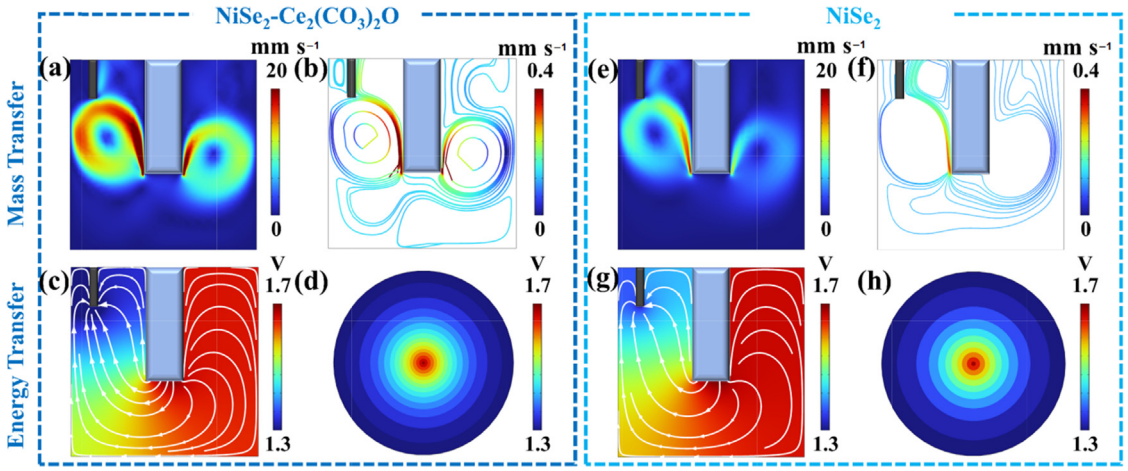

Fig. 3. FEM analysis on the OER performance of $NiSe_2$-$Ce_2(CO_3)_2O$ and $NiSe_2$ catalysts. Simulation result of the oxygen production rate for (a) $NiSe_2$-$Ce_2(CO_3)_2O$ and (e) $NiSe_2$. The surface tension of oxygen bubbles on the anodic (b) $NiSe_2$-$Ce_2(CO_3)_2O$ and (f) $NiSe_2$. The potentials and current density of electrolyte in the system of (c) $NiSe_2$-$Ce_2(CO_3)_2O$ and (g) $NiSe_2$. The current density distribution contour map for (d) $NiSe_2$-$Ce_2(CO_3)_2O$ and (h) $NiSe_2$.

trolyte. Therefore, a vortex caused by the different mass flow rates results in an eddy current near the electrode, further promoting mass transfer processes and improving OER performance. Virtually illustrated in Fig. 3(b and f), the surface tension of oxygen bubbles generated on the anodic $NiSe_2$-$Ce_2(CO_3)_2O$ surface is a more powerful driving force for fluid flow in the electrochemical reaction. Visibly, the size of the bubbles generated on the $NiSe_2$-$Ce_2(CO_3)_2O$ electrode surface accompanied with a smaller water contact angle, i.e. 16.4° versus 85.2° for $NiSe_2$-$Ce_2(CO_3)_2O$ and $NiSe_2$ (inset in Fig. 2e), was related to the hydrophilicity of the catalysts. The results revealed that the more hydrophilic the surface bubbles, the smaller the liquid driving force of the electrolytic cell was, which would facilitate the OER kinetic process. In terms of energy transfer, as shown in Fig. 3(c and g), the distribution of current density of electrolyte featured by white arrow line for $NiSe_2$-$Ce_2(CO_3)_2O$ is serried and extensive, suggesting more effectiveness on transportation of electrons in electrolyte for active $NiSe_2$-$Ce_2(CO_3)_2O$. Meanwhile, it is also speculated that the capability of acceleration of OER driven by $NiSe_2$-$Ce_2(CO_3)_2O$ in electrolyte involving electron transportation is more powerful since the potentials of electrolyte on surrounding of $NiSe_2$-$Ce_2(CO_3)_2O$ are more positive, leading to more intensive electron transfer. Additionally, we rotated the electrode surface along the normal direction to obtain the current density distribution contour map as shown in Fig. 3(d and h). It can be explained that the performance of the material is positively correlated with the contour density, indicating that $NiSe_2$-$Ce_2(CO_3)_2O$ with lower impedance and 2-times larger electrochemically active area has a better OER performance.

3.4. In situ characterization of structure and intermediate evolution

Regarding the dynamic reconstruction of catalysts prior to water oxidation, the redox electrochemistry of metal species in

various catalysts are explored, which are supposed to be decisive for forming active sites [48]. As displayed in CV scanning curves, the anodic oxidation peaks can be ascribed to by $Ni^{2+}\rightarrow Ni^{3+}$ oxidation, which signifies surface evolution into oxyhydroxides to offer the veritably active sites for OER [49,50]. The varied oxidation peaks for different catalysts imply their divergent evolution of Ni^{2+} species. As observed in Fig. 4(a), the peak for $NiSe_2$ underwent a positive shift compared to that of $NiSe_2$-$Ce_2(CO_3)_2O$, highlighting that the efficacy of $Ce_2(CO_3)_2O$ constituent in promoting the formation of Ni species with high-oxidation state [51]. Notably, the Ni oxidation peak for the $NiSe_2$-$Ce_2(CO_3)_2O$ was significantly larger than that of the $NiSe_2$, suggesting that a higher population of the active $Ni^{3+\delta}OOH$ species was formed [52,53]. We further leveraged potential-dependent in-situ Raman spectroscopy to confirm such a change of Ni^{2+}/Ni^{3+} electrochemical redox during OER process (The samples were not subjected to CV activation as for LSV measurements). As displayed in Fig. 4(b and c), the in-situ Raman spectra reveal the gradual disappearance of initial selenides and the concurrent emergence of NiOOH in both $NiSe_2$-$Ce_2(CO_3)_2O$ and $NiSe_2$ upon potential application. Two characteristic peaks of Ni^{3+}–O located at 472 and 554 cm^{-1} correspond to the E_g bending vibration and A_{1g} stretching vibration mode in NiOOH, respectively [54,55]. In-situ Raman spectroscopy suggested that the $NiSe_2$-$Ce_2(CO_3)_2O$ catalyst required a lower potential for the formation of Ni species with high-oxidation state compared to $NiSe_2$ catalyst. This result proves that the introduction of $Ce_2(CO_3)_2O$ component contributes to the phase evolution during electrochemical activation, thus oxygen evolution activity. The appearance of Raman signals closely parallels the anodic oxidation peaks in positive CV scanning curves, reiterating the dynamic reconstruction into oxyhydroxides.

To elucidate the charge transfer processes at the catalytic interface, in situ electrochemical impedance spectroscopy (EIS) measurements were carried out to detect dynamic evolution. As the potential increases, the size of the semicircle in the Nyquist plots significantly decreases, indicating the accelerated reaction kinetics and adsorption of reactants. As presented in Fig. S10(a and b), it is apparent that $NiSe_2$-$Ce_2(CO_3)_2O$ presents smaller charge transfer resistance at varying voltage levels compared with pure $NiSe_2$, suggesting that the heterostructure expedites charge transfer rate, which could promote surface activation of electrocatalyst [56,57]. Moreover, the EIS-derived Bode plot reflects both the dynamic evolution of electrocatalysts and OER process, exhibiting the variation of phase angle with frequency. The peak in the high-frequency region (10^2–10^5 Hz) is associated with the oxidation of the Ni species, whereas the peak in the low-frequency region (10^{-2}–10^1 Hz) is related to the OER [22,58]. The Bode plots of $NiSe_2$-$Ce_2(CO_3)_2O$ show that phase angles are smaller than those of $NiSe_2$ at each of the same applied potentials, indicating that more electrons are engaged in the OER catalysis, thereby improving the kinetics of the OER (Fig. 4d–f) [58–60]. In addition, Fig. 4(g) displays the interface dynamics process.

Based on the results of in situ Raman spectroscopy, $NiSe_2$-$Ce_2(CO_3)_2O$ has undergone self-reconstruction. We further re-examined the morphology and chemical environment of $NiSe_2$-$Ce_2(CO_3)_2O$ after OER stability test. As displayed in Fig. S11, the diffraction peak originally associated with $NiSe_2$ disappears in the XRD pattern, being replaced by the emergence of the diffraction peak of NiOOH. Noteworthily, the original $Ce_2(CO_3)_2O$ was stably maintained after stability test and was coupled with the reconstituted NiOOH. The Raman spectrum also exhibits peaks corresponding to NiOOH, which aligns with the XRD results (Fig. S12). Furthermore, the SEM (Fig. S13) indicates slight agglomeration on the surface morphology. The compositional change was further confirmed by high-resolution XPS spectra. The Ni 2*p* XPS spectrum of $NiSe_2$-$Ce_2(CO_3)_2O$ after OER presents that only the peak of Ni–O can be observed, indicating that all the surfaces of $NiSe_2$-$Ce_2(CO_3)_2O$ were oxidized to NiOOH (Fig. S14a) [61]. Additionally, Fig. S14(b) showcases almost no signals corresponding to Se atoms, pointing to the almost complete leaching of Se as previously reported [13]. The breaking of Ni–Se bond and the leaching of Se anions would bring about electronic structure rearrangement in metal center, consequently resulting a higher activity in derived-

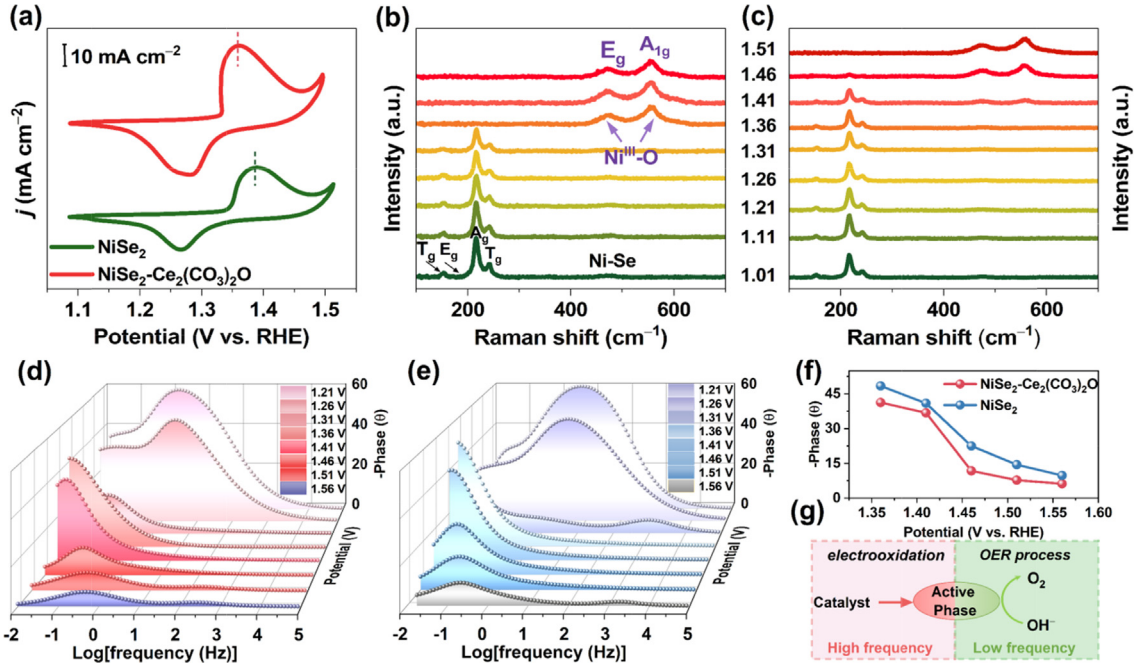

Fig. 4. Analysis of structural evolution process during OER. (a) Redox peaks of Ni in CV curves of $NiSe_2$-$Ce_2(CO_3)_2O$ and $NiSe_2$. Potential-dependent in situ Raman spectra of (b) $NiSe_2$-$Ce_2(CO_3)_2O$ and (c) $NiSe_2$ at different potentials (vs. RHE). Bode plots of (d) $NiSe_2$-$Ce_2(CO_3)_2O$ and (e) $NiSe_2$ at different potentials (vs. RHE). (f) Response of the phase angle to the applied potential. (g) Schematic diagram of interface dynamics process.

NiOOH [62]. As a result, in situ derived-NiOOH/$Ce_2(CO_3)_2O$ interfaces replace the pristine surface as the catalytically active species.

3.5. DFT calculation

To elucidate the relationship between the electronic structure and the OER catalytic mechanism, we performed first-principles calculations using density functional theory (DFT). To ensure the representation of the system, the derived-NiOOH/$Ce_2(CO_3)_2O$ is selected as computational model, aligning with the OER reaction process and comprehensive experimental results (Fig. S15a) [56]. In addition, pure NiOOH was also constructed as the counterpart (Fig. S15b). The differential charge density presents the charge accumulation around the Ni atoms in NiOOH at the interfacial region and the dispersion of electron states around the Ce atoms in $Ce_2(CO_3)_2O$, demonstrating significant electron interaction between NiOOH and $Ce_2(CO_3)_2O$ (Fig. 5a). A slice perspective of the differential charge density further provides a clearer view of this phenomenon, as illustrated in Fig. 5(b). This electron redistribution behavior can optimize the reaction intermediates absorption energy, thus enhancing the catalytic activity. We then analyzed the electronic structure of NiOOH/$Ce_2(CO_3)_2O$ by investigating the density of states (DOS). The total DOS displays that NiOOH/$Ce_2(CO_3)_2O$ possesses a higher electron density near the Fermi level than the NiOOH, indicating the enhanced electrical conductivity of NiOOH/$Ce_2(CO_3)_2O$ by coupling $Ce_2(CO_3)_2O$ (Fig. 5c) [63]. According to the *d*-band theory, the position of the *d*-band center (ε_d) reflected the binding strength of adsorption intermediate [64]. The ε_d of NiOOH/$Ce_2(CO_3)_2O$ is -1.15 eV, closer to the Fermi level than NiOOH (ε_d = -1.25 eV), indicating that the introduction of $Ce_2(CO_3)_2O$ can effectively optimize the electronic structure and *d*-band center of Ni sites, thereby enhancing the adsorption capacity of the materials to the intermediate. Generally, in alkaline environment, OER involves four-sequential proton-electron concerted processes accompanied with metal redox. Fig. 5(d) displays the OER pathways and optimized OER intermediate adsorption configurations for NiOOH/$Ce_2(CO_3)_2O$. The optimized adsorbed molecules are all found on the Ni sites, which are considered as adsorption sites for OER intermediates, in good accordance with the prior experimental results. To be precise, initially the metal bonded *OH species (where * refers to the metal sites) undergoes deprotonation upon reacting with an adsorbed OH^- species from the electrolyte, leading to the formation of *O. Next the *O would hybridize with one adsorbed OH^- to form *OOH, which is further deprotonated and transformed into an O_2 molecule [65,66]. Based on the four-electron transfer mechanism, the Gibbs free energy (*G*) was calculated for each basic step of OER, without the additional potential (*U* = 0). The rate-determining step (RDS) for both NiOOH/$Ce_2(CO_3)_2O$ and NiOOH is identified as the conversion step of *O to *OOH (Fig. 5e). NiOOH/$Ce_2(CO_3)_2O$ exhibits an *G* of 1.41 eV for the formation of *OOH, much lower than that of NiOOH (1.88 eV). The RDS of NiOOH/$Ce_2(CO_3)_2O$ undergoes a decrease, which explains the improved OER activity and indicates the critical role of $Ce_2(CO_3)_2O$ in enhancing activity. Overall, interfacial $Ce_2(CO_3)_2O$ can greatly optimize electronic structure of NiOOH/$Ce_2(CO_3)_2O$ and the Gibbs free energy of OER pathways, thereby boosting electrocatalytic activity.

3.6. Overall water splitting

Such excellent OER performance propels us to assemble a water-alkali electrolyzer to evaluate its potential for practical overall water splitting. A two-electrode water electrolyzer was constructed by paring the homemade $NiSe_2$-$Ce_2(CO_3)_2O$ anode with Pt/C cathode (marked as $NiSe_2$-$Ce_2(CO_3)_2O^{(+)}$||Pt/$C^{(-)}$). A reference cell with commercial Pt/C and RuO_2 as cathode and anode, respectively, was also tested for comparison (marked as $RuO_2^{(+)}$||Pt/$C^{(-)}$) (Fig. 6a). The polarization curve of the $NiSe_2$-$Ce_2(CO_3)_2O^{(+)}$||Pt/$C^{(-)}$ cell presents excellent overall water splitting performance in 1.0 M KOH electrolyte (Fig. 6b). In detail, Fig. 6(c) shows the comparison of voltages at different current densities. The $NiSe_2$-$Ce_2(CO_3)_2O^{(+)}$||Pt/$C^{(-)}$ cell possesses smaller voltages of 1.65, 1.75,

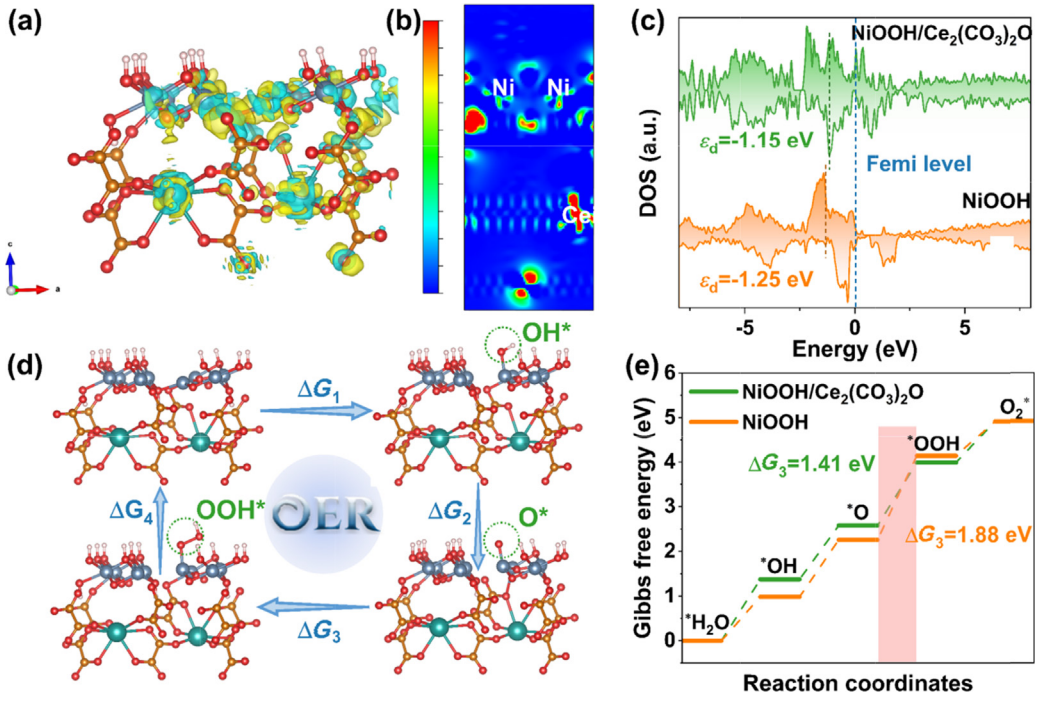

Fig. 5. DFT calculations. (a) Differential charge density of NiOOH/$Ce_2(CO_3)_2O$, the yellow and blue zones represent the charge accumulation and dispersion, respectively. (b) 2D charge difference isosurface based on DFT analysis, red is the electron-rich area while blue is the deficient area. (c) The DOS plots of NiOOH/$Ce_2(CO_3)_2O$ and NiOOH. (d) OER mechanism illustration of NiOOH/$Ce_2(CO_3)_2O$. (e) Gibbs free energy diagrams of NiOOH/$Ce_2(CO_3)_2O$ and NiOOH.

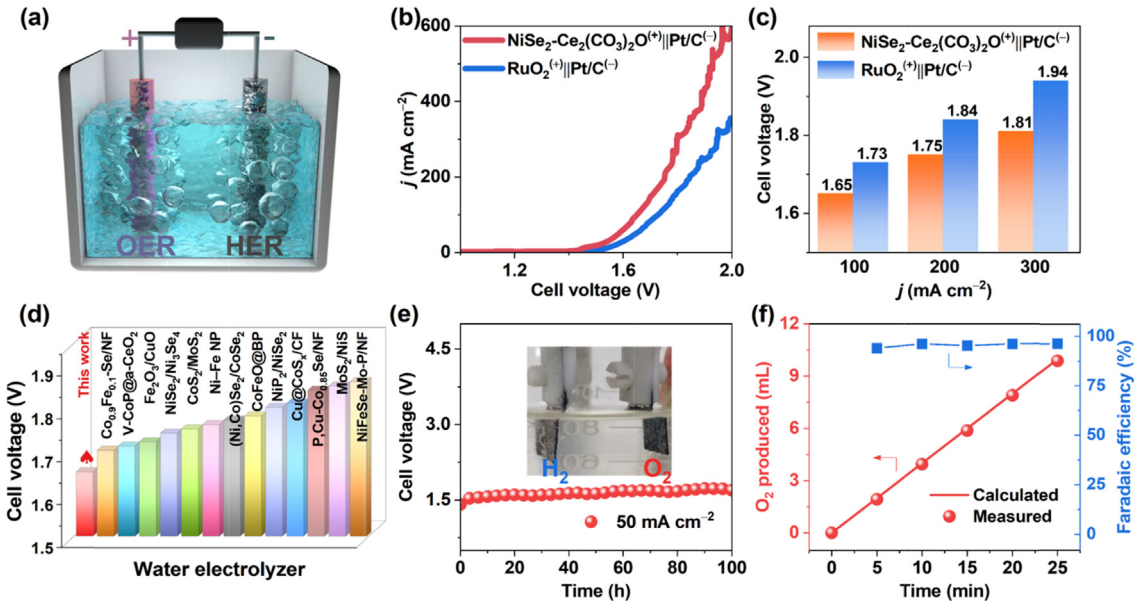

Fig. 6. Overall water splitting performance of the $NiSe_2$-$Ce_2(CO_3)_2O$ catalyst in 1.0 M KOH. (a) Schematic description of overall water splitting in two-electrode system. (b) Polarization curves of the electrolytic cells with $NiSe_2$-$Ce_2(CO_3)_2O^{(+)}||Pt/C^{(-)}$ and the reference cell with $RuO_2^{(+)}||Pt/C^{(-)}$. (c) Comparison of the required voltages at different current densities. (d) Comparison the cell voltage at 100 mA cm^{-2} with previously reported catalysts. (e) Chronopotentiometry curves at 50 mA cm^{-2} (inset: experimental phenomenon during catalyst stability test). (f) Faradaic efficiency measurement for OER.

and 1.81 V to reach 100, 200, and 300 mA cm^{-2}, respectively, in comparison with the $RuO_2^{(+)}||Pt/C^{(-)}$ (1.73, 1.84, and 1.94 V). Meanwhile, compared with recently reported noble-metal-free electrocatalysts for overall water splitting, our cell performance at high current density (1.65 V at 100 mA cm^{-2}) stands competitively, as depicted in Fig. 6(d) and Table S3. The long-term stability of $NiSe_2$-$Ce_2(CO_3)_2O^{(+)}||Pt/C^{(-)}$ is also a critical checkpoint for its practical utilization. The continuous operation at 50 mA cm^{-2} indicates that the cell voltage shows imperceptible attenuation in 100 h, suggesting its superior durability (Fig. 6e). As illustrated in Fig. 6(f) and Fig. S16, the Faradaic efficiency (FE) for $NiSe_2$-$Ce_2(CO_3)_2O$ demonstrated close to 100%, as determined by comparing the experimentally obtained oxygen volume with the theoretical expectation [67]. These merits indicate that activated $NiSe_2$-$Ce_2(CO_3)_2O$ exhibits exceptional catalytic activity for overall water splitting, which makes it a highly propitious alternative for developing efficient and cost-effective water splitting technologies.

4. Conclusions

In summary, we have successfully synthesized $NiSe_2$-$Ce_2(CO_3)_2O$ heterostructure on carbon cloth with high performance toward OER. In/ex-situ characterizations and density functional theory calculations are utilized to analyze the dynamic structural evolution and the relationship between the self-reconstruction and the catalytic performance. Concretely, the generation potential of highly active NiOOH is effectively reduced by incorporating $Ce_2(CO_3)_2O$ into the $NiSe_2$ catalyst. The charge transfer processes at the catalytic interface are significantly enhanced by the heterostructure, leading to accelerated reaction kinetics and improved mass transfer rates. Moreover, DFT calculations verify that the interfacial $Ce_2(CO_3)_2O$ is critical in optimizing the *d*-band center and facilitating the adsorption of oxygen-containing intermediates on active centers, thus significantly improving the OER activity. The resultant catalyst has emerged as an efficient OER electrocatalyst, requiring a low overpotential of 268 mV at 50 mA cm^{-2} and being maintained continuously for 120 h without significant attenuation observed. This work provides new insights into promoting the formation of actual active species for efficient OER activity.

CRediT authorship contribution statement

Fengli Wei: Writing – original draft, Investigation, Conceptualization. **Jinghao Shen:** Investigation. **Jiayin Xie:** Data curation. **Zuyang Luo:** Methodology. **Luyan Shi:** Data curation. **Tayirjan Taylor Isimjan:** Writing – review & editing. **Xiulin Yang:** Writing – review & editing, Supervision. **Jieshan Qiu:** Writing – review & editing, Supervision. **Bin Wu:** Writing – review & editing.

Declaration of competing interest

The authors declare that they have no known competing financial interests or personal relationships that could have appeared to influence the work reported in this paper.

Acknowledgments

This work was financially supported by the National Natural Science Foundation of China (52363028, 21965005), the Volkswagen Foundation (Freigeist Fellowship 89592), the Natural Science Foundation of Guangxi Province (2021GXNSFAA076001), the Guangxi Technology Base and Talent Subject (GUIKE AD23023004, GUIKE AD20297039), and Innovation Project of Guangxi Graduate Education (Nos. YCSW2024219, YCBZ2024082).

Appendix A. Supplementary material

Supplementary data to this article can be found online at https://doi.org/10.1016/j.jechem.2024.06.048.

References

[1] K. Shah, R. Dai, M. Mateen, Z. Hassan, Z. Zhuang, C. Liu, M. Israr, W.C. Cheong, B. Hu, R. Tu, C. Zhang, X. Chen, Q. Peng, C. Chen, Y. Li, Angew. Chem. Int. Ed. 61 (2022) e202114951.

[2] H. Wang, Z.N. Chen, D. Wu, M. Cao, F. Sun, H. Zhang, H. You, W. Zhuang, R. Cao, J. Am. Chem. Soc. 143 (2021) 4639–4645.
[3] R. Mehmood, W. Fan, X. Hu, J. Li, P. Liu, Y. Zhang, Z. Zhou, J. Wang, M. Liu, F. Zhang, J. Am. Chem. Soc. 145 (2023) 12206–12213.
[4] Y. Ou, L.P. Twight, B. Samanta, L. Liu, S. Biswas, J.L. Fehrs, N.A. Sagui, J. Villalobos, J. Morales-Santelices, D. Antipin, M. Risch, M.C. Toroker, S.W. Boettcher, Nat. Commun. 14 (2023) 7688.
[5] F. Wei, J. Shen, J. Gong, Q. Peng, L. Shi, T.T. Isimjan, X. Yang, J. Phys. Chem. Lett. 15 (2024) 1172–1180.
[6] Z. Luo, Q. Peng, Z. Huang, L. Wang, Y. Yang, J. Dong, T.T. Isimjan, X. Yang, J. Colloid Interface Sci. 629 (2023) 111–120.
[7] S. Jayachitra, D. Mahendiran, P. Ravi, P. Murugan, M. Sathish, Appl. Catal. B Environ. Energy 307 (2022) 121159.
[8] M. Li, L. Feng, Chinese J. Struc. Chem. 41 (2022) 2201019–2201024.
[9] H. Lei, L. Ma, Q. Wan, S. Tan, B. Yang, Z. Wang, W. Mai, H.J. Fan, Adv. Energy Mater. 12 (2022) 2202522.
[10] Y. Shi, W. Du, W. Zhou, C. Wang, S. Lu, S. Lu, B. Zhang, Angew. Chem. Int. Ed. 59 (2020) 22470–22474.
[11] X. Liu, J. Meng, J. Zhu, M. Huang, B. Wen, R. Guo, L. Mai, Adv. Mater. 33 (2021) 2007344.
[12] S. Niu, W.-J. Jiang, Z. Wei, T. Tang, J. Ma, J.-S. Hu, L.-J. Wan, J. Am. Chem. Soc. 141 (2019) 7005–7013.
[13] X. Xu, F. Song, X. Hu, Nat. Commun. 7 (2016) 12324.
[14] C. Lin, J.-L. Li, X. Li, S. Yang, W. Luo, Y. Zhang, S.-H. Kim, D.-H. Kim, S.S. Shinde, Y.-F. Li, Z.-P. Liu, Z. Jiang, J.-H. Lee, Nat. Catal. 4 (2021) 1012–1023.
[15] T. Wu, S. Sun, J. Song, S. Xi, Y. Du, B. Chen, W.A. Sasangka, H. Liao, C.L. Gan, G.G. Scherer, L. Zeng, H. Wang, H. Li, A. Grimaud, Z.J. Xu, Nat. Catal. 2 (2019) 763–772.
[16] Y. Chang, Z. Ma, X. Lu, S. Wang, J. Bao, Y. Liu, C. Ma, Angew. Chem. Int. Ed. 62 (2023) e202310163.
[17] R. Liu, M. Sun, X. Liu, Z. Lv, X. Yu, J. Wang, Y. Liu, L. Li, X. Feng, W. Yang, B. Huang, B. Wang, Angew. Chem. Int. Ed. 62 (2023) e202312644.
[18] Y. Zeng, M. Zhao, Z. Huang, W. Zhu, J. Zheng, Q. Jiang, Z. Wang, H. Liang, Adv. Energy Mater. 12 (2022) 2201713.
[19] L. Xu, R. Iqbal, Y. Wang, S. Taimoor, L. Hao, R. Dong, K. Liu, J. Texter, Z. Sun, The Innovation Materials 2 (2024) 100060.
[20] X. Xu, H. Liao, L. Huang, S. Chen, R. Wang, S. Wu, Y. Wu, Z. Sun, H. Huang, Appl. Catal. B Environ. Energy 341 (2024) 123312.
[21] M. Jiang, H. Zhai, L. Chen, L. Mei, P. Tan, K. Yang, J. Pan, Adv. Fun. Mater. 33 (2023) 2302621.
[22] Y. Li, Y. Wu, M. Yuan, H. Hao, Z. Lv, L. Xu, B. Wei, Appl. Catal. B Environ. Energy 318 (2022) 121825.
[23] G. Li, P. Wang, M. He, X. Yuan, L. Tang, Z. Li, Sci. China Chem. 66 (2023) 2204–2220.
[24] H. Liu, J. Yu, C. Qiu, R. Yu, S. Li, J. Cheng, J. Wang, Z. Si, S. Yang, Funct. Mater. Lett. 14 (2021) 2130009.
[25] X. Ding, R. Jiang, J. Wu, M. Xing, Z. Qiao, X. Zeng, S. Wang, D. Cao, Adv. Fun. Mater. 33 (2023) 2306786.
[26] S.F. Zai, X.Y. Gao, C.C. Yang, Q. Jiang, Adv. Energy Mater. 11 (2021) 2101266.
[27] Z. Huang, X. Liao, W. Zhang, J. Hu, Q. Gao, ACS Catal. 12 (2022) 13951–13960.
[28] T. Dai, X. Zhang, M. Sun, B. Huang, N. Zhang, P. Da, R. Yang, Z. He, W. Wang, P. Xi, C.H. Yan, Adv. Mater. 33 (2021) 2102593.
[29] S. Yin, Y. Minamidate, S. Tonouchi, T. Goto, Q. Dong, H. Yamane, T. Sato, RSC Adv. 2 (2012) 5976–5982.
[30] L. Wang, M. Huang, M. Gao, T.T. Isimjan, X. Yang, Mater. Chem. Front. 7 (2023) 2628–2636.
[31] Y. Chen, J. Wang, Z. Yu, Y. Hou, R. Jiang, M. Wang, J. Huang, J. Chen, Y. Zhang, H. Zhu, Appl. Catal. B Environ. Energy 307 (2022) 121151.
[32] C. Gu, S. Hu, X. Zheng, M.R. Gao, Y.R. Zheng, L. Shi, Q. Gao, X. Zheng, W. Chu, H. B. Yao, J. Zhu, S.H. Yu, Angew. Chem. Int. Ed. 57 (2018) 4020–4024.
[33] C. Liu, Y. Han, L. Yao, L. Liang, J. He, Q. Hao, J. Zhang, Y. Li, H. Liu, Small 17 (2021) 2007334.
[34] L. Shi, K. Zhu, Y. Yang, Y. Liu, S. Xu, T.T. Isimjan, X. Yang, Int. J. Hydrogen Energy 47 (2022) 37840–37849.
[35] Y. Wang, S. Hao, X. Liu, Q. Wang, Z. Su, L. Lei, X. Zhang, ACS Appl. Mater. Interfaces 12 (2020) 37006–37012.
[36] T. Wu, S. Xu, Z. Zhang, M. Luo, R. Wang, Y. Tang, J. Wang, F. Huang, Adv. Sci. 9 (2022) 2202750.
[37] M. Ahmad, B. Xi, Y. Gu, H. Zhang, S. Xiong, Inorg. Chem. Front. 9 (2022) 448–457.
[38] Z. Liu, D. Wang, Z. Liu, W. Li, R. Zhang, L. Wu, H. Mu, Y. Hou, Q. Gao, L. Feng, G. Wen, J. Colloid Interface Sci. 627 (2022) 716–729.
[39] L. Wang, Y. Hao, L. Deng, F. Hu, S. Zhao, L. Li, S. Peng, Nat. Commun. 13 (2022) 5785.
[40] Y. Zuo, S. Bellani, G. Saleh, M. Ferri, D.V. Shinde, M.I. Zappia, J. Buha, R. Brescia, M. Prato, R. Pascazio, A. Annamalai, D.O. de Souza, L. De Trizio, I. Infante, F. Bonaccorso, L. Manna, J. Am. Chem. Soc. 145 (2023) 21419–21431.
[41] L. Wang, M. Ma, C. Zhang, H.-H. Chang, Y. Zhang, L. Li, H.-Y. Chen, S. Peng, Angew. Chem. Int. Ed. 63 (2023) e202317220.
[42] Q. Peng, X. Zhuang, L. Wei, L. Shi, T.T. Isimjan, R. Hou, X. Yang, ChemSusChem 15 (2022) e202200827.
[43] Q. Ji, Y. Kong, H. Tan, H. Duan, N. Li, B. Tang, Y. Wang, S. Feng, L. Lv, C. Wang, F. Hu, W. Zhang, L. Cai, W. Yan, ACS Catal. 12 (2022) 4318–4326.
[44] N. Zhang, C. Deng, S. Tao, L. Guo, Y. Cheng, Chem. Eng. Sci. 224 (2020) 115795.
[45] J. Zhao, Q. Li, Q. Zhang, R. Liu, Chem. Eng. J. 431 (2022) 133730.
[46] A.P. O'Mullane, J. Phys. Energy 2 (2020) 041001.
[47] R. Shi, L. Shang, C. Zhou, Y. Zhao, T. Zhang, Exploration 2 (2022) 20210046.
[48] S.A. Chala, M.-C. Tsai, B.W. Olbasa, K. Lakshmanan, W.-H. Huang, W.-N. Su, Y.-F. Liao, J.-F. Lee, H. Dai, B.J. Hwang, ACS Nano 15 (2021) 14996–15006.
[49] N. Zhang, X. Feng, D. Rao, X. Deng, L. Cai, B. Qiu, R. Long, Y. Xiong, Y. Lu, Y. Chai, Nat. Commun. 11 (2020) 4066.
[50] R.R. Rao, S. Corby, A. Bucci, M. Garcia-Tecedor, C.A. Mesa, J. Rossmeisl, S. Gimenez, J. Lloret-Fillol, I.E.L. Stephens, J.R. Durrant, J. Am. Chem. Soc. 144 (2022) 7622–7633.
[51] J. Ding, D. Guo, N. Wang, H.-F. Wang, X. Yang, K. Shen, L. Chen, Y. Li, Angew. Chem. Int. Ed. 62 (2023) e202311909.
[52] H. Liao, G. Ni, P. Tan, Y. Liu, K. Chen, G. Wang, M. Liu, J. Pan, Appl. Catal. B Environ. Energy 317 (2022) 121713.
[53] T. Zhao, X. Shen, Y. Wang, R.K. Hocking, Y. Li, C. Rong, K. Dastafkan, Z. Su, C. Zhao, Adv. Funct. Mater. 31 (2021) 2100614.
[54] Z.-H. Yin, Y. Huang, K. Song, T.-T. Li, J.-Y. Cui, C. Meng, H. Zhang, J.-J. Wang, J. Am. Chem. Soc. 146 (2024) 6846.
[55] N. Zhang, Y. Hu, L. An, Q. Li, J. Yin, J. Li, R. Yang, M. Lu, S. Zhang, P. Xi, C.H. Yan, Angew. Chem. Int. Ed. 61 (2022) e202207217.
[56] P. Zhai, C. Wang, Y. Zhao, Y. Zhang, J. Gao, L. Sun, J. Hou, Nat. Commun. 14 (2023) 1873.
[57] Y. Hao, S.-F. Hung, C. Tian, L. Wang, Y.-Y. Chen, S. Zhao, K.-S. Peng, C. Zhang, Y. Zhang, C.-H. Kuo, H.-Y. Chen, S. Peng, Angew. Chem. Int. Ed. 63 (2024) e202402018.
[58] S. Zhou, H. He, J. Li, Z. Ye, Z. Liu, J. Shi, Y. Hu, W. Cai, Adv. Fun. Mater. 34 (2023) 2313770.
[59] X. Lei, C. Jiang, Q. Han, X. Zhang, K. Zhao, N. Yan, H. Guo, B. Tang, Y. Li, Y. Cui, X.-Z. Fu, J. Li, Y. Sun, ACS Catal. 14 (2024) 4523–4535.
[60] Z. Du, Z. Meng, X. Gong, Z. Hao, X. Li, H. Sun, X. Hu, S. Yu, H. Tian, Angew. Chem. Int. Ed. 63 (2023) e202317022.
[61] X. Liu, S. Cao, J. Li, Y. Wang, W. Xue, G. Liu, Small 19 (2023) 2304652.
[62] X. Chen, Z. Qiu, H. Xing, S. Fei, J. Li, L. Ma, Y. Li, D. Liu, Appl. Catal. B Environ. Energy 305 (2022) 121030.
[63] S. Zhang, Z. Huang, T.T. Isimjan, D. Cai, X. Yang, Appl. Catal. B Environ. Energy 343 (2024) 123448.
[64] Y. Yang, L. Shi, Q. Liang, Y. Liu, J. Dong, T.T. Isimjan, B. Wang, X. Yang, Chin. J. Catal. 56 (2024) 176–187.
[65] H. Zhong, Q. Zhang, J. Yu, X. Zhang, C. Wu, Y. Ma, H. An, H. Wang, J. Zhang, X. Wang, J. Xue, Adv. Energy Mater. 13 (2023) 2301391.
[66] Y. Hu, Z. Luo, M. Guo, J. Dong, P. Yan, C. Hu, T.T. Isimjan, X. Yang, Chem. Eng. J. 435 (2022) 134795.
[67] B. Cui, Z. Hu, C. Liu, S. Liu, F. Chen, S. Hu, J. Zhang, W. Zhou, Y. Deng, Z. Qin, Z. Wu, Y. Chen, L. Cui, W. Hu, Nano Res. 14 (2020) 1149–1155.